Journal of Materials Chemistry A

PAPER

View Article Online
View Journal | View Issue

Cite this: J. Mater. Chem. A, 2017, 5, 18120

Boundary layer tuning induced fast and high performance perovskite film precipitation by facile one-step solution engineering†

Li-Li Gao, Ke-Jie Zhang, Ni Chen and Guan-Jun Yang *

Received 9th June 2017
Accepted 31st July 2017

DOI: 10.1039/c7ta05012g

rsc.li/materials-a

As promising highly-efficient and low-cost photovoltaic devices, perovskite solar cells must be made of compact and pin-hole free perovskite films. One-step solution engineering is a most efficient and low-cost precipitation of high quality perovskite films. However, the difficulty in controlling the precipitation and pin-hole formation in perovskite films makes this one-step solution engineering a great challenge. Here, we report, for the first time, a fast and high performance perovskite film precipitation by tuning the boundary layer during the solution processing of the perovskite film. Theoretical analyses and simulations were carried out alongside the experiments, and the results consistently showed that a high velocity and low temperature of the air flow could effectively reduce the thickness of the boundary layer. Subsequently, evaporated solvent molecules would diffuse through the boundary layer more easily, and then solvent evaporation becomes quicker, resulting in a high quality and pin-hole free perovskite film. As a result, the highest efficiency of 17.87% was achieved for planar perovskite solar cells (with an active area of 0.1 cm^2) with the perovskite film precipitated under these air conditions. Furthermore, the efficiency reached as high as 12.72% with a 1.08 V open-circuit voltage for a 1 cm^2 planar perovskite device. This essentially opens the door to developing high quality perovskite film precipitation approaches by tuning the boundary layer during facile one-step solution engineering.

Introduction

Perovskite solar cells (PSCs) are promising low-cost photovoltaic devices with high solar-to-electric power conversion efficiencies (PCEs). In recent reports there has been an unprecedented rapid increase in PCEs, providing a new promising path to industrial scale production. The advances are mainly attributed to the excellent optoelectronic properties and easy processing of hybrid perovskite materials, such as $MAPbI_3$ and $FAPbI_3$ and their blends (where MA = methylammonium and FA = formamidinium cations).[1–4] Additionally, perovskite device architectures can be flexibly designed in normal (n-type layer at the front) or inverted (p-type layer at the front) assemblies with mesoscopic or planar heterojunction structures,[5] where the perovskite layer is always sandwiched between the electron transport layers (ETLs) and hole transport layers (HTLs).[6–10] Regardless of the device configuration, the quality of the perovskite light harvesting layer is of critical importance to obtain a high efficiency.[11–15]

As the crucial layer, the crystallinity, morphology, thickness, and surface coverage of the perovskite film are the primary factors influencing the photovoltaic performance.[12,16,17] Fast one-step film precipitation is the most efficient and low-cost way to prepare the perovskite film, which is one promising route to the industrialization of PSCs.[18] However, the organo-lead halide perovskite films made by one-step solution engineering present micro-sized branch-like crystals and large uncovered areas. As a result, the HTL and ETL contact each other directly, leading to a localized short circuit and a low efficiency.[12,19] Therefore, various methods based on solution-processing have been provided to deposit perovskite films,[4,20,21] such as air-assisted drying[22,23] and anti-solvent management, in which crystallization is induced by virulent chlorobenzene.[19,24] Actually, the essence of all the methods is the fast precipitation of the solute on the perovskite solution film. Therefore, the key issue is tuning fast precipitation, namely, controlling the process of fast solvent evaporation. In conventional drying, heating drying and air-assisted drying, the most difficult step is the diffusion of solvent molecules at the interface of the liquid perovskite film (Scheme 1). Interface diffusion of evaporated solvent molecules is essential for the precipitation of lots of crystal nuclei, such as in air-assisted drying. The slow diffusion of solvent molecules at the surface of the perovskite solution film in natural drying and heating drying results in the branch-like morphology. Thereby, the interface of the perovskite solution film is critical for one-step solution engineering. However, a comprehensive and critical

State Key Laboratory for Mechanical Behavior of Materials, School of Materials Science and Engineering, Xi'an Jiaotong University, Xi'an, Shaanxi 710049, PR China. E-mail: ygj@mail.xjtu.edu.cn

† Electronic supplementary information (ESI) available. See DOI: 10.1039/c7ta05012g

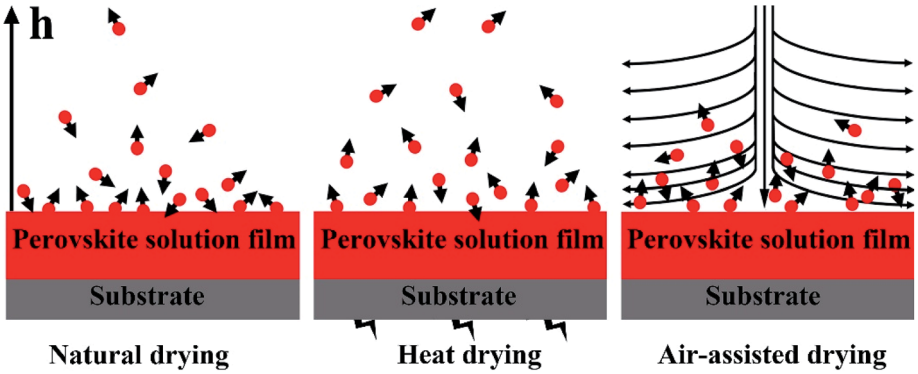

Scheme 1 The diffusion of natural drying, heating drying and air-assisted drying at the interface of the perovskite solution film (*h* is the diffusion distance).

study of the interface between the air and solution film surface has never been reported until now.

Based on fluid mechanics,[25,26] there is always a boundary layer as long as a two-phase interface exists, even in the natural environment. The boundary layer is the thin transition region which arises due to fluid viscosity and interface friction. In the present study, we aimed to study the boundary layer located at the interface between the perovskite solution film and the air flow. Generally, the evaporation involves three consecutive steps. Firstly, the solvent molecules evaporate from the solution surface and transform into a gaseous phase. Secondly, these gaseous solvent molecules diffuse through the boundary layer under the concentration gradient. Finally, once the solvent molecules have left the boundary layer, they will be taken away by strong air convection. During air assisted drying, the diffusion process in the boundary layer is extremely slow, which makes it the controlling step of the whole evaporation process. Therefore, understanding and tailoring the boundary layer is vital for promoting solvent evaporation.

Apparently, an evaporated gaseous solvent molecule diffuses more easily through a thinner boundary layer. In this manuscript, we aim to tune the thickness of the boundary layer and accelerate solvent evaporation using our previously reported multi-flow air knife (MAK).[27] Based on fluid mechanics, air flow velocity and air temperature are two important parameters which affect the boundary layer thickness. According to theoretical analyses, simulations and experiments, a faster air velocity and a lower air temperature will result in a thinner boundary layer. Due to the fast solvent evaporation, a compact and smooth thin perovskite film forms. At last, planar heterojunction perovskite-based solar cells employing pin-hole free perovskite films were fabricated with active areas of 1 cm^2. The highest efficiency has reached 12.72% with an open circuit voltage up to 1.08 V and the high performance can be attributed to the excellent film quality.[28,29]

Results and discussion

Fast solvent diffusion in the boundary layer

In order to make the evaporated solvent molecules diffuse effectively, we must have a comprehensive understanding of the boundary layer. The air flow can be divided into a free stream area and a boundary layer area. According to fluid mechanics, the boundary layer thickness is the vertical distance from the solution surface to a point where the flow velocity has essentially reached the "free stream" velocity, as shown in Fig. S1.† The partition of the boundary layer and the free stream is the point where the velocity reaches a certain value (generally 99%) of the free stream velocity, while a different partition can be defined for certain research. The boundary layer can be divided into laminar flow and turbulent flow. The air velocity in the turbulent region is much larger than that in the laminar region. Therefore, we define, in this study, that the critical gas velocity is 60% of the free stream velocity, which contains the laminar region and has significant influence on the diffusion of molecules. No matter where the partition is, the air velocity in the boundary layer is much lower than that in the free stream area. Actually, the macroscopic flow velocity of the air molecules in the boundary layer close to the solution surface is nearly zero and there's only microscopic molecular thermodynamic movement left. The immobilized air molecules act as a huge obstacle for evaporated gaseous solvent molecules. Therefore, it's a challenge for the evaporated solvent molecules to diffuse from the boundary layer to the free stream where the molecules can be effectively taken away by the high-speed air flow.

Fig. 1a shows the scheme of the boundary layer between the air flow and the solution film surface. When the air flow sweeps the solution perovskite film surface, the boundary layer will generate simultaneously. Gases close to the solution film surface tend to be of a very low velocity because of the viscous effects and friction between the gas and solution surface. The velocity of the gas far away from the solution film surface tends to become slightly faster. In the direction perpendicular to the solution surface, the velocity of the air flow increases until reaching the maximum value in the free stream region. Fig. 1b shows the process of the evaporation. Firstly, the liquid phase transforms to a gas, then the gas molecules diffuse in the boundary layer, and finally the gas molecules are taken away by convection. Based on fluid mechanics, the diffusion of gas molecules in the boundary layer is very slow, which is the controlling step of the whole evaporation process. In order to

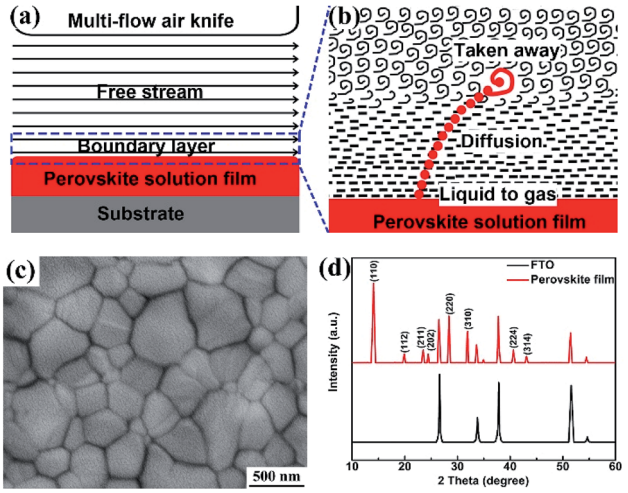

Fig. 1 (a) Schematic illustration of the boundary layer between the perovskite solution film and the air flow, (b) schematic illustration of a solvent molecule across the boundary layer, (c) SEM surface morphology of an air-flow dried perovskite film, and (d) XRD patterns of the $CH_3NH_3PbI_3$ film deposited on an FTO glass substrate.

guarantee sufficient evaporation, evaporated solvent molecules must diffuse quickly across the boundary layer, thus reducing the boundary layer thickness is an effective option.

Fig. 1c shows the morphology of the perovskite film, which was dried by air flow with a velocity of 45.87 m s^{-1} (corresponding to an air flow of 350 L min^{-1}) and temperature of 20 °C. The film is compact and pin-hole free over the whole area. Flat polygonal grains with triple junction grain boundaries are the predominant microstructural features, which suggests the close packing of perovskite grains over the whole area. Fig. S2† shows the grain size distribution from a statistical measurement of 500 grains. It reveals a mean size of 356 ± 41 nm and that 90% of the grains range from 200 to 500 nm. The crystalline structure of the $CH_3NH_3PbI_3$ perovskite film on the FTO substrate is characterized by X-ray diffraction (XRD) (see Fig. 1d). Sharp diffraction peaks at 14.08°, 28.40°, and 31.83° are clearly observed corresponding to the (110), (220), and (310) crystallographic planes, respectively, revealing the presence of the $CH_3NH_3PbI_3$ tetragonal phase (space group $I4/mcm$, $a = b =$ 8.8743 Å, and c = 12.6708 Å).[30] Furthermore, the optical properties of the perovskite film, such as the ultraviolet-visible absorption, transmission and reflection, are also identified. The film absorbs a wide range of light from the visible range to the near-infrared range, showing remarkable intensity at *ca.* 500 nm (see Fig. S3a†) which indicates the successful formation of the $CH_3NH_3PbI_3$ perovskite on the substrate. The result is in good consistency with the report in the literature.[31] Accordingly, the absorption, transmission and reflection proportions are also shown in Fig. S3b.† In the wavelength range of 380–550 nm, without transmission, almost 80% of the light is absorbed. Above 550 nm, absorption begins to decrease and transmission increases, while reflection is almost unchanged in the whole range of detected wavelengths. The excellent optical properties are probably due to the low defect density in the bulk of the perovskite film.[12,19,32]

Calculation on the boundary layer

In order to achieve a thin boundary layer to realize efficient solvent evaporation in a short time, the boundary layer thickness has to be tuned effectively. To reduce the boundary layer effectively, we first calculated the boundary layer thickness based on the empirical formula

$$\delta = \frac{L}{\sqrt{\mathrm{Re}}} \quad (1)$$

where δ is the boundary layer thickness, L is the distance of the air flow sweep at the solution surface (parallel to the surface in this case) and in this experiment L is equal to the solution surface length. Re is the Reynolds number. Based on eqn (1), the boundary layer thickness relies on Re, which dictates

$$\mathrm{Re} = \frac{\rho v d}{\eta} \quad (2)$$

where ρ, v, d and η are the gas density, gas velocity, characteristic length (here, d represents the solution surface length, equal to L numerically), and gas viscosity coefficient, respectively. When the inertia force of the air flow is much larger than its viscidity force, the boundary layer tends to be very thin. The inertia force depends on the fluid velocity and density, while the viscidity force mainly depends on the fluid viscidity. The fluid density and viscidity rely on the fluid temperature. Air flow viscidity will enlarge and air flow density will decrease as the temperature increases, as shown in Fig. S4.† Therefore, based on eqn (2), in order to make the boundary layer as thin as possible, a large velocity air flow with a low temperature should be adopted to dry the perovskite solution film.

Based on eqn (1), we calculated the boundary layer thickness with various air temperatures and velocities. The detailed parameters are listed in Table S1.† The direct variation is shown in Fig. 2. As the air velocity increases and the air temperature decreases, the boundary layer thickness reduces gradually (see the red arrows). The influence of air velocity on the boundary layer thickness is significant, and the boundary layer thickness reduces to nearly one third of its initial value when the air velocity increases from 6.55 to 45.87 m s^{-1} (air flow increasing from 50 to 350 L min^{-1}). However, the influence of the air temperature is minor as the boundary layer thickness reduces only slightly even though the air flow temperature increases from 20 to 150 °C. Therefore, increasing the air velocity properly at room temperature is a sustainable and feasible way to reduce the boundary layer thickness to promote solvent molecule diffusion.

Simulation on boundary layer

In order to observe the boundary layer thickness vividly, we conducted a simulation on the air flow. First, we drew a schematic diagram of one unit multi-flow air knife drying (Fig. S5a†), and divided the calculation area into a mesh (Fig. S5b†) to simulate the air velocity distribution using fluent software and get the thickness of the boundary layer.

In order to observe the influence of the distances between the air flow and solution film on the boundary layer thickness,

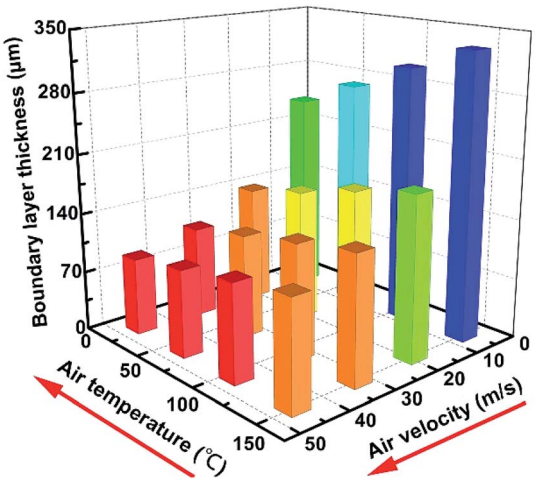

Fig. 2 Boundary layer thickness variation with various air temperatures and air velocities.

several distinct distances were simulated with the same air velocity (45.87 m s^{-1}). We can clearly observe the air velocity distribution in the calculation area (Fig. 3a–d) and the detailed air velocity distribution at the bottom of air flow (Fig. 3e–h). With the distance decreasing, particularly on reducing to 1 mm, the boundary layer thickness reduces greatly, as shown in Fig. 3i. The low distance is favourable for evaporated solvent molecule diffusion with a great concentration gradient, which is in good consistency with our previous report.[33] Therefore, it illustrates that reducing the distance between the air flow and the solution film surface is a better way to decrease the boundary layer thickness (Table 1).

However, further decreasing the distance between the air flow and the solution film surface from 1 mm is difficult to realize. Thereby, it is necessary to use another method to reduce the boundary layer thickness. Fortunately, we can further reduce the boundary layer thickness by controlling the air flow parameters. We set the distance to 1 mm and the simulation about the boundary layer brought about by air velocity variation and air temperature variation is shown in Fig. 4. It can be concluded from the simulations that the boundary layer thickness reduces greatly to thirty percent of the original value with an increasing air velocity from 6.55 to 45.87 m s^{-1} (air flow increasing from 50 to 350 L min^{-1}), as shown in Fig. 4a–e. In addition, the boundary layer thickness reduces slightly when the air flow temperature decreases from 150 to 20 °C, as shown in Fig. 4f–j. Therefore, increasing the air velocity can reduce the boundary layer thickness enormously. The influence of air temperature is slight and so room temperature is an effective choice for air drying. The simulation results (Fig. 4) are in good consistency with the above calculations (Fig. 2).

Experiments on the boundary layer: dependence of the perovskite film quality on the boundary layer thickness

To investigate the effect of the perovskite film microstructure and the boundary layer thickness, we dried perovskite films at different boundary layer thicknesses. We change the boundary

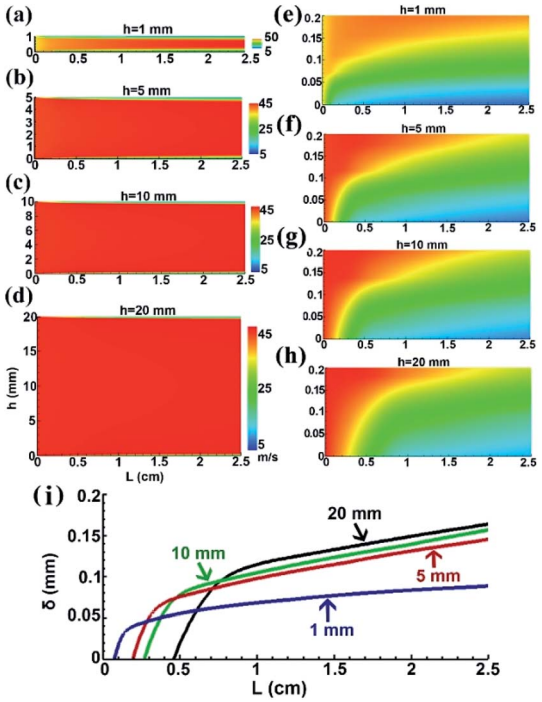

Fig. 3 Air velocity magnitude with different distances between the air flow and the solution film surface: (a) 1 mm, (b) 5 mm, (c) 10 mm and (d) 20 mm; (e–h) the local high magnification of the bottom air flow of (a–d) respectively. (i) is the boundary layer thickness variation within the distance of the air flow sweeping the solution surface.

layer thickness by controlling two main processing parameters, *i.e.*, air velocity and temperature. After being dried at an air velocity of 45.87 m s^{-1} (350 L min^{-1}) and a temperature of 20 °C, where the boundary layer thickness is about 90 μm, the perovskite film became black-brown transparent with a mirror-like surface. When the air flow velocity was lower than 45.87 m s^{-1} or the air temperature higher than 20 °C, where the boundary layer becomes thicker, the dried perovskite film became blurry and opaque. To quantitatively investigate their microscopic morphology and surface quality, SEM and AFM were conducted on a randomly chosen large and uniform perovskite film.

Firstly, the influence of the boundary layer thickness on the film morphology was explored by controlling the air velocity. When increasing the air velocity with a constant air temperature of 20 °C, the perovskite films acquired a more compact and smooth morphology. Fig. 5a shows the SEM morphology and AFM images of the film dried at 6.55 m s^{-1} (50 L min^{-1}). Large rod-like grains and some pin-holes are visible and the grain sizes reach tens of micrometers. Some substrates are uncovered by perovskite grains. Huge fluctuations and bare substrates can also be seen on the AFM and 3D images and the root mean square (RMS) roughness is 95.6 nm. From the cross sectional image (Fig. S6a†), the thickness of the dendritic grains is about 680 nm. When the air velocity increases to 19.66 m s^{-1} (150 L min^{-1}), the rod-like grains decrease to several micrometers and the pin-hole sizes also reduce enormously. The film surface becomes smoother with the air flow velocity increasing.

Table 1 The definitions of L, δ and h in Fig. 3 and 4

Parameters	Definition
L	The distance of the air flow sweeping the solution surface
δ	The boundary layer thickness
h	The distance between the air flow and the solution film surface

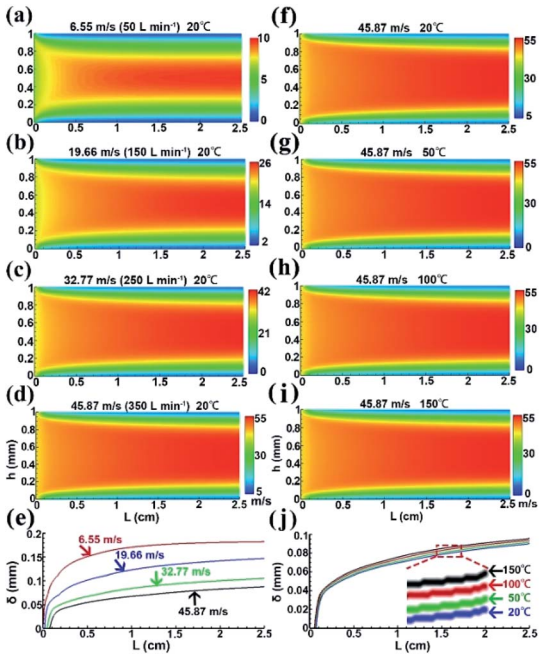

Fig. 4 The magnitude of the air flow velocity with distinct air velocities and distinct air temperatures. (a–d) are the velocity magnitudes with distinct air velocities at 20 °C, (f–i) are the velocity magnitudes with distinct air temperatures at 45.87 m s^{-1}, (e) is the boundary layer thickness variation with distinct air velocities at 20 °C and (j) is the boundary layer thickness variation with distinct air temperatures at 45.87 m s^{-1}.

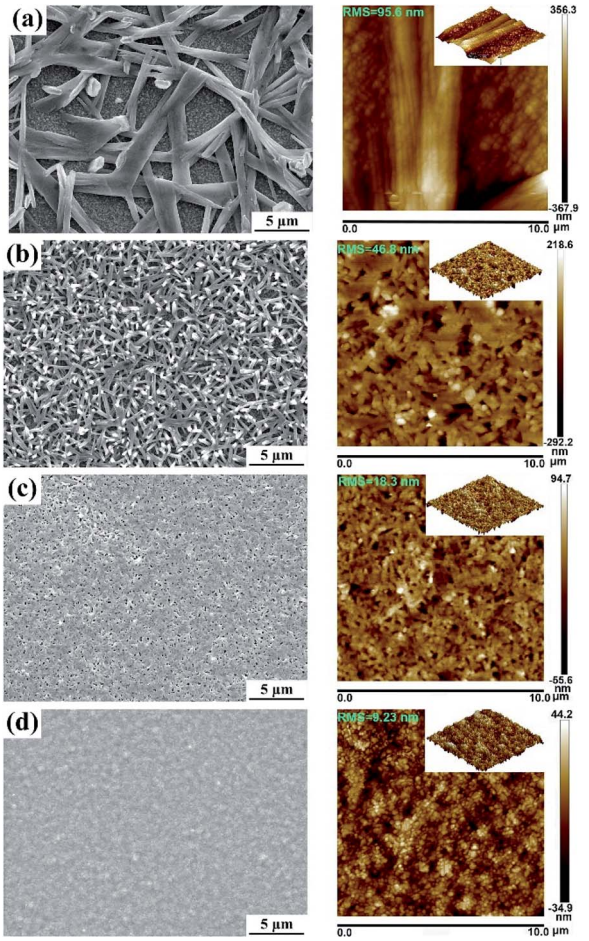

Fig. 5 SEM surface morphologies and AFM images of the perovskite film dried at 20 °C with varied air flow velocities: (a) 6.55 m s^{-1} (50 L min^{-1}), (b) 19.66 m s^{-1} (150 L min^{-1}), (c) 32.77 m s^{-1} (250 L min^{-1}) and (d) 45.87 m s^{-1} (350 L min^{-1}). The inset is the 3D image.

The RMS roughness reduces to 46.8 nm (see Fig. 5b). The perovskite film shows grains of hundreds of nanometers and the pin-hole sizes reduce to about five hundred nanometers when the air velocity increases to 32.77 m s^{-1} (250 L min^{-1}). The film thickness also reduces from 320 to 242 nm (Fig. S6b and c†). The AFM results show that the film becomes much smoother as the RMS roughness reduces to 18.3 nm, as shown in Fig. 5c. Finally, with the air velocity increasing to 45.87 m s^{-1} (350 L min^{-1}), the perovskite film displays an extremely compact and pin-hole free morphology and the RMS roughness is 9.23 nm, fluctuations can hardly be seen in Fig. 5d, and the cross sectional image shows close-packed columnar grains with a thickness of 240 nm (Fig. S6d†). In summary, with the air velocity increasing, the boundary layer thickness reduces, and the dried perovskite films evolve from a blurred to a mirror-like morphology, as shown in Fig. S8a.† The experimental results (Fig. 5) are in good consistency with the calculations (Fig. 2) and simulations (Fig. 4) above. Therefore, it can be concluded that increasing the air velocity is an effective way to reduce the boundary layer thickness, which contributes to the diffusion of solvent molecules and accelerates the solvent evaporation rate.

In addition, the boundary layer thickness can be tuned by changing the air temperature. We examined the surface morphologies of the perovskite films obtained at different air temperatures. With a fixed air velocity of 45.87 m s^{-1} (350 L min^{-1}), we increase the air temperature from 20 to 150 °C. At room temperature, the perovskite film is very smooth and compact and the AFM result shows that the RMS roughness is 9.25 nm (Fig. 6a, measured from the same sample as in Fig. 5d but in a different area). Some slight pits started emerging in the film when it was dried by a 50 °C air flow, as shown in Fig. 6b. The RMS roughness increases a little to 13.3 nm. The pits evolve into pin-holes when the air temperature increases to 100 °C, with a RMS roughness of 14.6 nm in Fig. 6c. The pin-holes become a little more numerous and larger at an air temperature of 150 °C, and the RMS roughness is 15.5 nm in Fig. 6d. Also the cross section images do not show very big differences (Fig. S7a to d†). From all of the above

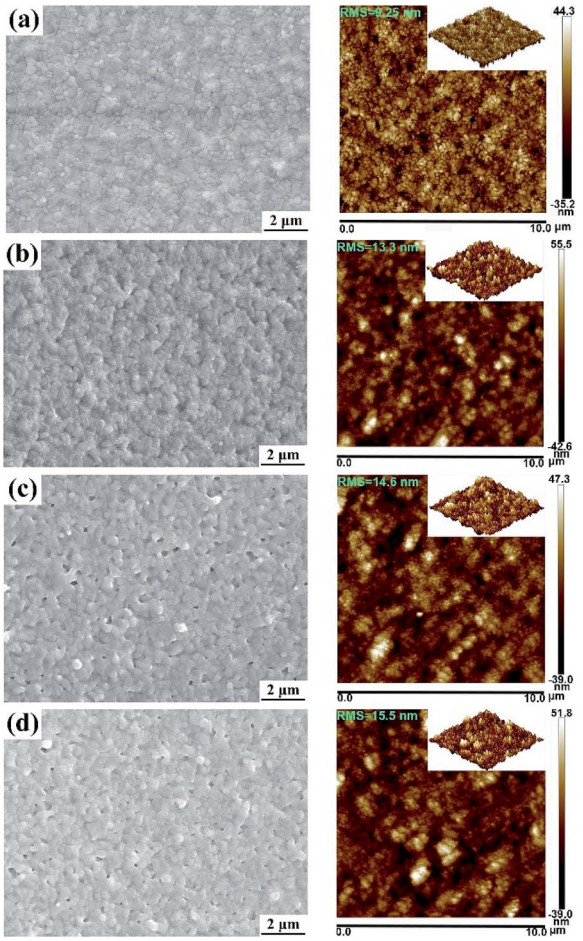

Fig. 6 SEM surface morphologies and AFM images of the perovskite film dried at 350 L min^{-1} with different air-flow temperatures: (a) 20 °C, (b) 50 °C, (c) 100 °C and (d) 150 °C. The inset is the 3D image.

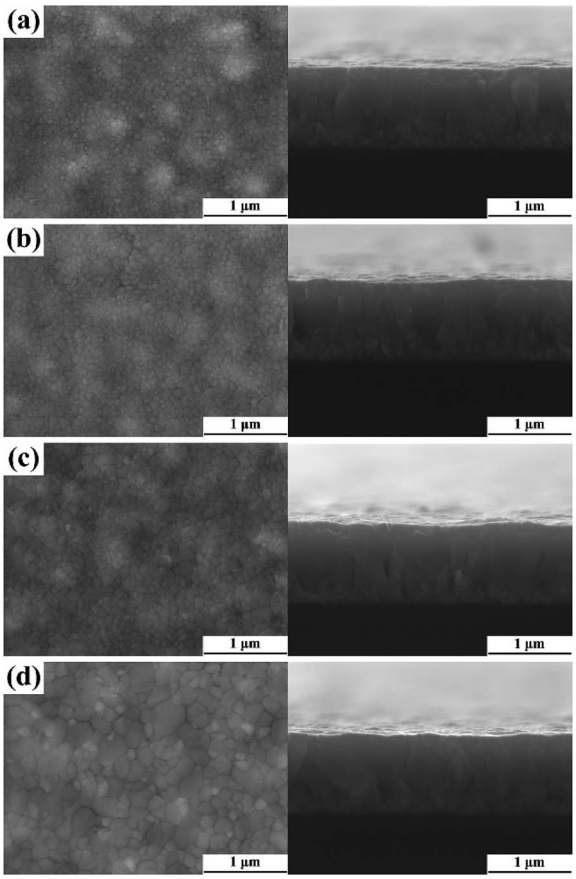

Fig. 7 SEM morphologies of the perovskite films annealed at different temperatures for 10 min: (a) 0 °C, (b) 50 °C, (c) 100 °C and (d) 150 °C.

results, the morphology variation with increasing air temperature is not very clear. Obvious features cannot be observed with the naked eye, as shown in Fig. S8b.† The film morphologies vary slightly with increasing air temperature, the reason being that the variations of the boundary layer are not very evident. The experiment results (Fig. 6) are in good consistency with the calculations (Fig. 2) and simulations (Fig. 4). Therefore, a low temperature air flow is more favorable for perovskite film drying because it reduces the boundary layer thickness and improves the solvent evaporation rate.

In order to investigate the effect of subsequent annealing on the perovskite films, Fig. 7 shows the SEM morphologies of the perovskite films annealed at different temperatures. The dried film without annealing already exhibits obvious grains (Fig. 7a). The XRD result further confirms the good crystallinity of the film without the annealing process (Fig. S9†). It indicates that the initial crystal growth of the compact perovskite film has already occurred during the drying process rather than in the subsequent annealing treatment. It can be seen that the grains grow from 100 nm to 400 nm on increasing the annealing temperature from 0 to 150 °C. After being annealed at 150 °C, a phase of PbI_2 appears (Fig. S9†). Therefore, annealing at 100 °C is considered to be the optimum to obtain a good crystallinity. Devices employing this annealing condition will be discussed subsequently.

Photovoltaic performance of the perovskite solar cells

In order to investigate the effects of the perovskite film morphology on the device performance, the final planar heterojunction perovskite-based solar cells were fabricated with an active area of 1 and 0.1 cm^2. The perovskite films were dried at different air velocities and temperatures. However, only the perovskite film dried at 20 °C with an air velocity of 45.87 m s^{-1} (350 L min^{-1}) provides the best efficiency, and the device electrical properties are shown in Fig. 8.

Fig. 8a shows the cross-sectional SEM image of the PSC using an air-flow-dried perovskite film. A 50 nm compact TiO_2 layer is deposited on a 500 nm FTO substrate working as the positive electrode. The hybrid structured perovskite is used as the active layer, which consists of an ~300 nm thick perovskite. The spiro-oMeTAD HTM layer of less than 50 nm thick lies next to the perovskite capping layer and Au metal is finally deposited as the photocathode. The best *J–V* curves of the devices fabricated with an active area of 1 cm^2 employing air flow dried perovskite films are shown in Fig. 8b. Under simulated air-mass (AM) 1.5 sun light, the device exhibited a promising PCE of 12.72% with

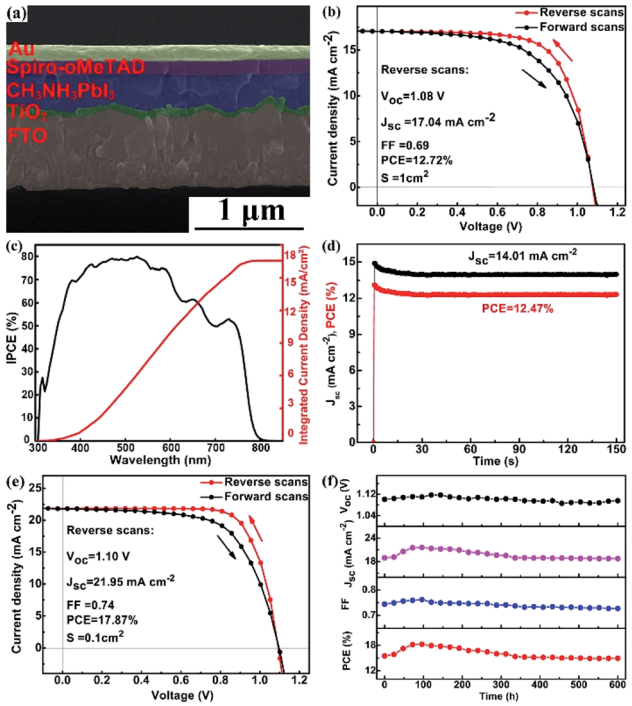

Fig. 8 (a) Cross-sectional SEM image of the perovskite solar cell, (b) *J–V* curve of the device with an active area of 1 cm^2 and (c) its corresponding IPCE spectra, (d) the steady-state current density and power conversion efficiency, (e) the best *J–V* curve of the device with an active area of 0.1 cm^2, and (f) its stability with time.

a short circuit current density (J_{sc}) of 17.04 mA cm^{-2} and a fill factor (FF) of 0.69. It's worth noting that the open circuit voltage (V_{oc}) is 1.08 V, which is comparatively high for such a large active device area. It illustrates that the perovskite film is compact over the whole active area, and thus presents excellent electrical performance. Fig. 8c shows its corresponding incident photon-to-current conversion efficiency (IPCE) spectrum and the integrated current density as a function of the wavelength. The IPCE spectrum reveals that the device has a spectral response from the visible to near infrared region (300–800 nm) with a peak IPCE of nearly 80% at approximately 500 nm. The IPCE spectrum of the device is coincident with the UV-vis spectrum of the $CH_3NH_3PbI_3$ perovskite film as illustrated in Fig. S3a.† This observation suggests that the $CH_3NH_3PbI_3$ perovskite acts as the light absorber and is the primary contributor to the photocurrent. The integral J_{sc} is 16.54 mA cm^{-2}, which is roughly comparable with those obtained from the *J–V* curves. To determine a more realistic efficiency of the device by considering the hysteresis effect, a steady state PCE was measured at its maximum power point as a function of time at the forward bias of 0.89 V, as shown in Fig. 8d. Under 1 sun continuous illumination, the steady-state photocurrent density stabilized at 14.01 mA cm^{-2}, and the power conversion efficiency (PCE) stabilized at 12.47% over 150 s. In order to reveal the underlying carrier transport behavior in the perovskite solar cells, electronic impedance spectroscopy (EIS) measurements were performed from 4 MHz to 0.1 Hz at a forward bias of 1.0 V under illumination by a monochromatic light source. There are two semicircles in the Nyquist plot, as shown in Fig. S10.† The left small semicircle corresponding to the high frequency comes from the resistance of the charge transfer at the counter electrode together with transport through the hole conductor, R_t. The right big semicircle corresponding to the low frequency is related to the resistance of the charge carrier recombination at the interfaces between the perovskite and charge extraction layers, R_{re}.[5,34,35] The equivalent circuit that fits the experimental data is shown in the inset of Fig. S10.† Based on the fitting, R_t is 3.23 kΩ and R_{re} is 20.45 kΩ, which illustrates that a small charge transfer resistance and a large charge carrier recombination resistance are required for better photocurrent output.

Furthermore, some comparative devices were also fabricated. The *J–V* curves are shown in Fig. S11.† Because of the discontinuous perovskite film dried by low air velocity, the device efficiencies are unsatisfactory. The perovskite film coverage and device efficiencies increase with an increasing drying air velocity, as shown in Fig. S11a.† The perovskite film coverage decreases slightly when the air temperature increases from 20 to 150 °C and the device efficiencies vary slightly, as shown in Fig. S11b.† As well as the influence of film coverage, the film grain size arising due to the annealing temperature also affects the device performance. When the grain size is larger than 200 nm, the applied devices achieve a high efficiency, as shown in Fig. S11c.† The influence of the film morphology on the device performance is illustrated clearly and is in good consistency with the reported results.[12,20,24]

In addition, another device with an active area of 0.1 cm^2 was also measured to have a high efficiency of 17.87% (Fig. 8e), and the corresponding IPCE spectrum is shown in Fig. S12a.† In spite of the high efficiency, another major concern is device durability for application.[36,37] Thereby, the unencapsulated device stability was monitored by testing in an ambient environment at 20 ± 5 °C with a 20–25% humidity under the same measuring conditions. It can be seen from Fig. 8f that the V_{oc} is always stable at around 1.10 V without decay up to 600 hours, which can be attributed to the compact perovskite film dried by a high air velocity and a low temperature air flow. The J_{sc}, FF and PCE were also stable up to 600 hours with values of 18.75 mA cm^{-2}, 0.73, and 14.94%, respectively. The compact perovskite film was also measured by XRD and the patterns shown in Fig. S12b† illustrate that there is no decomposition for nearly a month. Furthermore, the devices show excellent reproducibility, and the statistical data on the device performances based on 100 devices are shown in Fig. S13.† More than 80% of the device efficiencies are higher than 15%. Overall, the compact perovskite film contributes to the device high efficiency, good stability and reproducibility in ambient air.

Conclusions

In summary, the boundary layer is the controlling step for the perovskite solution film evaporation process. The theoretical analyses and simulations are in good consistency with the experimental results which enable us to conclude that a high air velocity and a low air temperature help accelerate the solvent evaporation process by reducing the boundary layer thickness.

Under the condition of a suitable air velocity of 45.87 m s^{-1} (350 L min^{-1}) at 20 °C, we have produced uniform, pin-hole free and rough-border-free perovskite films with a large crystal grain size. In addition, planar perovskite solar cells with an active area of 1 and 0.1 cm^2 containing the fabricated films exhibit the highest efficiencies of 12.72% and 17.87%, respectively. We believe that a detailed and comprehensive understanding of the boundary layer is essential for tuneable perovskite solvent film evaporation, and provides a broad view for solution processes fabricating high-quality perovskite films by adopting low cost and facile one-step air flow drying methods.

Acknowledgements

The authors acknowledge the financial support from the National Program for Support of Top-notch Young Professionals. They also thank Mr Jie Liu and Ms Nan Zhu for the IPCE and AFM testing.

References

1 T. Y. Hsieh, C. K. Huang, T. S. Su, C. Y. Hong and T. C. Wei, *ACS Appl. Mater. Interfaces*, 2017, **9**, 8623–8633.
2 M. Saliba, T. Matsui, J.-Y. Seo, K. Domanski, J.-P. Correa-Baena, M. K. Nazeeruddin, S. M. Zakeeruddin, W. Tress, A. Abate and A. Hagfeldt, *Energy Environ. Sci.*, 2016, **9**, 1989–1997.
3 G. E. Eperon, S. D. Stranks, C. Menelaou, M. B. Johnston, L. M. Herz and H. J. Snaith, *Energy Environ. Sci.*, 2014, **7**, 982–988.
4 Y. Y. Zhou, M. J. Yang, A. L. Vasiliev, H. F. Garces, Y. X. Zhao, D. Wang, S. P. Pang, K. Zhu and N. P. Padture, *J. Mater. Chem. A*, 2015, **3**, 9249–9256.
5 D. Li, J. Cui, H. Li, D. K. Huang, M. K. Wang and Y. Shen, *Sol. Energy*, 2016, **131**, 176–182.
6 J. Burschka, N. Pellet, S. J. Moon, R. Humphry-Baker, P. Gao, M. K. Nazeeruddin and M. Gratzel, *Nature*, 2013, **499**, 316–320.
7 Y. Dkhissi, S. Meyer, D. H. Chen, H. C. Weerasinghe, L. Spiccia, Y. B. Cheng and R. A. Caruso, *Chemsuschem*, 2016, **9**, 687–695.
8 Q. Shen, Y. Ogomi, J. Chang, T. Toyoda, K. Fujiwara, K. Yoshino, K. Sato, K. Yamazaki, M. Akimoto, Y. Kuga, K. Katayama and S. Hayase, *J. Mater. Chem. A*, 2015, **3**, 9308–9316.
9 L. Cojocaru, S. Uchida, A. K. Jena, T. Miyasaka, J. Nakazaki, T. Kubo and H. Segawa, *Chem. Lett.*, 2015, **44**, 1089–1091.
10 Y. K. Kim, U. Thakur, B. Jeon and H. J. Park, *J. Phys. Chem. C*, 2017, **121**, 3161.
11 J. H. Heo, D. H. Song and S. H. Im, *Adv. Mater.*, 2014, **26**, 8179–8183.
12 G. E. Eperon, V. M. Burlakov, P. Docampo, A. Goriely and H. J. Snaith, *Adv. Funct. Mater.*, 2014, **24**, 151–157.
13 N. Ahn, D. Y. Son, I. H. Jang, S. M. Kang, M. Choi and N. G. Park, *J. Am. Chem. Soc.*, 2015, **137**, 8696–8699.
14 S. Yuan, Z. W. Qiu, C. M. Gao, H. L. Zhang, Y. A. Jiang, C. C. Li, J. H. Yu and B. Q. Cao, *ACS Appl. Mater. Interfaces*, 2016, **8**, 22238–22245.
15 B. Li, J. J. Tian, L. X. Guo, C. B. Fei, T. Shen, X. H. Qu and G. Z. Cao, *ACS Appl. Mater. Interfaces*, 2016, **8**, 4684–4690.
16 J. Feng and B. Xiao, *J. Phys. Chem. Lett.*, 2014, **5**, 1719–1720.
17 J. Kim, J. S. Yun, X. M. Wen, A. M. Soufiani, C. F. J. Lau, B. Wilkinson, J. Seidel, M. A. Green, S. J. Huang and A. W. Y. Ho-Baillie, *J. Phys. Chem. C*, 2016, **120**, 11262–11267.
18 H. P. Xie, X. L. Liu, L. Lyu, D. M. Niu, Q. Wang, J. S. Huang and Y. L. Gao, *J. Phys. Chem. C*, 2016, **120**, 215–220.
19 M. D. Xiao, F. Z. Huang, W. C. Huang, Y. Dkhissi, Y. Zhu, J. Etheridge, A. Gray-Weale, U. Bach, Y. B. Cheng and L. Spiccia, *Angew. Chem., Int. Ed.*, 2014, **53**, 9898–9903.
20 F. X. Xie, D. Zhang, H. Su, X. Ren, K. S. Wong, M. Grätzel and W. C. Choy, *ACS Nano*, 2015, **9**, 639–646.
21 Q. Chen, H. Zhou, Z. Hong, S. Luo, H.-S. Duan, H.-H. Wang, Y. Liu, G. Li and Y. Yang, *J. Am. Chem. Soc.*, 2013, **136**, 622–625.
22 K. Hwang, Y. S. Jung, Y. J. Heo, F. H. Scholes, S. E. Watkins, J. Subbiah, D. J. Jones, D. Y. Kim and D. Vak, *Adv. Mater.*, 2015, **27**, 1241–1247.
23 Y. Dkhissi, F. Huang, S. Rubanov, M. Xiao, U. Bach, L. Spiccia, R. A. Caruso and Y.-B. Cheng, *J. Power Sources*, 2015, **278**, 325–331.
24 N. J. Jeon, J. H. Noh, Y. C. Kim, W. S. Yang, S. Ryu and S. I. Seok, *Nat. Mater.*, 2014, **13**, 897–903.
25 H. Schlichting and K. Gersten, in *Boundary-Layer Theory*, Springer, 2017, pp. 29–49.
26 H. Schlichting and K. Gersten, *J. Fluid Mech.*, 2017, **20**, 48–89.
27 L. L. Gao, C. X. Li, C. J. Li and G. J. Yang, *J. Mater. Chem. A*, 2017, **5**, 1548–1557.
28 J. Song, E. Zheng, J. Bian, X.-F. Wang, W. Tian, Y. Sanehira and T. Miyasaka, *J. Mater. Chem. A*, 2015, **3**, 10837–10844.
29 E. Zheng, X. F. Wang, J. Song, L. Yan, W. Tian and T. Miyasaka, *ACS Appl. Mater. Interfaces*, 2015, **7**, 18156–18162.
30 T. Baikie, Y. Fang, J. M. Kadro, M. Schreyer, F. Wei, S. G. Mhaisalkar, M. Graetzel and T. J. White, *J. Mater. Chem. A*, 2013, **1**, 5628–5641.
31 O. Malinkiewicz, A. Yella, Y. H. Lee, G. M. Espallargas, M. Graetzel, M. K. Nazeeruddin and H. J. Bolink, *Nat. Photonics*, 2014, **8**, 128–132.
32 Z. Wang, J. Cui, J. Li, K. Cao, S. Yuan, Y. Cheng and M. Wang, *Mater. Sci. Eng., B*, 2015, **199**, 1–8.
33 L.-L. Gao, C. Li, C. Li and G.-J. Yang, *J. Mater. Chem. A*, 2017, **5**, 1548–1557.
34 M. J. Yang, R. Guo, K. Kadel, Y. Y. Liu, K. O'Shea, R. Bone, X. W. Wang, J. He and W. Z. Li, *J. Mater. Chem. A*, 2014, **2**, 19616–19622.
35 C. Sun, Z. H. Wu, H. L. Yip, H. Zhang, X. F. Jiang, Q. F. Xue, Z. C. Hu, Z. H. Hu, Y. Shen, M. K. Wang, F. Huang and Y. Cao, *Adv. Energy Mater.*, 2016, **6**, 1501534.
36 J. W. Lee, D. H. Kim, H. S. Kim, S. W. Seo, S. M. Cho and N. G. Park, *Adv. Energy Mater.*, 2015, **5**, 1501310.
37 A. Bera, A. D. Sheikh, M. A. Haque, R. Bose, E. Alarousu, O. F. Mohammed and T. Wu, *ACS Appl. Mater. Interfaces*, 2015, **7**, 28404–28411.